crystals

MDPI

Article

Stable $CsPbBr_3$ Nanocrystals—Decorated Nanoporous Gold for Optoelectronic Applications

Jessica Satta [1,*], Andrea Pinna [2], Giorgio Pia [2], Luca Pilia [2], Carlo Maria Carbonaro [1], Daniele Chiriu [1], Luigi Stagi [3], Qader Abdulqader Abdullah [4] and Pier Carlo Ricci [1]

1 Department of Physics, Campus of Monserrato, University of Cagliari, SP n.8, km 0.700, 09042 Monserrato, Italy; cm.carbonaro@dsf.unica.it (C.M.C.); daniele.chiriu@dsf.unica.it (D.C.); carlo.ricci@dsf.unica.it (P.C.R.)
2 Department of Mechanical, Chemical and Materials Engineering, University of Cagliari, Via Marengo, 2, 09123 Cagliari, Italy; andrea.pinna@dsf.unica.it (A.P.); giorgio.pia@dimcm.unica.it (G.P.); pilialuc@unica.it (L.P.)
3 Laboratory of Materials Science and Nanotechnology, CR-INSTM, Department of Chemistry and Pharmacy, University of Sassari, Via Vienna 2, 07100 Sassari, Italy; lstagi@uniss.it
4 Department of Physics, University of Sulaimani, Kirkuk Road, Sulaimani 46001, Kurdistan Region, Iraq; abdulqader.qader@univsul.edu.iq
* Correspondence: jessica.satta@dsf.unica.it

Abstract: Halide perovskite colloidal nanocrystals have recently gained much attention thanks to their superior stability compared with their bulk counterpart and to their unique optical properties. In this paper, two systems combining nanocrystals and nanoporous gold are studied to create an optimal metal semiconductor heterojunction that can be used in photocatalysis and photovoltaic devices. The perovskite degradation phenomenon is observed when the nanoporous gold powder is mixed into the hexane suspension of nanocrystals, while the charge separation efficiency is increased by synthesizing the nanocrystals directly onto the gold porous structure. The analysis of the structural and optical properties evidences an energy transfer efficiency of 47%, along with the high structural stability of the hybrid system.

Keywords: lead halide perovskites; nanoporous gold; metal semiconductor heterostructure; charge transfer

Citation: Satta, J.; Pinna, A.; Pia, G.; Pilia, L.; Carbonaro, C.M.; Chiriu, D.; Stagi, L.; Abdullah, Q.A.; Ricci, P.C. Stable $CsPbBr_3$ Nanocrystals—Decorated Nanoporous Gold for Optoelectronic Applications. *Crystals* **2022**, *12*, 863. https://doi.org/10.3390/cryst12060863

Academic Editor: Dmitri Donetski

Received: 9 May 2022
Accepted: 14 June 2022
Published: 18 June 2022

1. Introduction

Since the 1990s, halide perovskites nanocrystals (NCs) have received increasing attention in an optoelectronic context for their intrinsic properties, finding potential applications in many different sectors and devices ranging from efficient light harvesters to photovoltaics, photodetectors, solar fuels, lighting, and displays [1]. Despite their promising characteristics, the efficiency of perovskite-based devices is far from the theoretically predicted values, probably due to poor charge transfer at the interfaces [2,3]. Further, their poor stability hampers the commercial applications of the devices, being sensitive to heat, light, and environmental stresses [4–7]. In photocatalysis and photovoltaics, for example the performance of the devices depends on their charge separation ability and the implementation of good NCs-electrode interfaces. The development of nanocrystal-metal heterostructures can help to improve both factors and provide new functionalities to the nanostructures, altering the optical properties of the semiconductors, notably with photoluminescence quenching or enhancement [8–10]. Noble metals are widely used for their intrinsic capacity to accept electrons, quickly capturing the photogenerated electrons at the semiconductor surface and promoting the charge separation and reduction processes. The presence of metal is also known to induce plasmonic field effects in semiconductor nanostructures, influencing their photocatalytic and photovoltaic performances [11,12]. Previously, several studies have been focused on the optical properties of lead halide perovskite-Au nanocomposites and their application in photocatalysis and photovoltaics [13–15]. In particular,

Liao et al. recently reported that $CsPbBr_3$ nanocrystals coupled with plasmonic Au nanoparticles (NPs) showed dramatically enhanced charge separation, which resulted in a 3.2-fold enhancement in the photocatalytic activity of CO_2 [14]. The authors also found that hot electrons produced via localized surface plasmon resonance (LSPR) in Au NPs could be transferred to the NCs and contribute to the CO_2 reduction. However, such systems can suffer from the typical nanoparticle drawbacks, such as their agglomeration and the need for a substrate in which they can be anchored [16].

In this framework, nanoporous (NP) metals could represent an intriguing alternative for preparing efficient self-supported metal–perovskite heterojunctions, which could be particularly suitable for advanced photoelectrodes. Indeed, three-dimensional (3D) interconnected porous structures have higher surface areas than photoelectrodes made from 1D arrays of nanoparticles, decreasing the electron pathways and with that the electron–hole recombination probability [17–19]. Being made of interconnected nano–sized ligaments and pores, NP metals are commonly obtained by dealloying a precursor alloy [16] and they present the common properties of bulk metals associated with enhancements related to their high surface area, low density, and plasmonic and catalytic activities. NP metals find possible applications in various technological areas [16], such as catalysis [20], sensing [21], surface-enhanced Raman spectroscopy (SERS) [22], metal-enhanced fluorescence (MEF) [23], actuators [24], and energy storage and conversion [25]. Nanoporous gold (hereafter, NP Au) represents the most studied and promising material thanks to its low reactivity and its efficient fabrication from Au-Ag precursor alloys.

Among the vast field of applications, NP Au-semiconductor composites have shown promising synergic enhancement of photocatalytic properties, thanks to the enhanced electron–hole pair generation and charge separation, resulting in enhanced photocurrent and catalytic activity levels. NP Au-CdS flexible photoelectrodes showed enhanced hydrogen evolution rates and photostability in CdS nanolayers [19]. Similarly, Jia et al. reported the enhanced photoelectrocatalytic activity of TiO_2 NP-decorated NP Au towards methanol oxidation [26]. Moreover, NP Au thin films were also proven to be efficient back electrodes of hole-transport-material-free perovskite solar cells [15].

In this work, we explored the possibility to develop a $CsPbBr_3$-NP Au heterostructure (hereafter NCs@NP Au). Indeed, two different approaches were developed and studied to obtain the NCs-NP Au system, and the optical and structural properties are reported. By analyzing the effect on the optical properties of $CsPbBr_3$ influenced by the presence of gold, we evidence the efficient charge transfer process in NCs@NP Au, investigating the possible mechanisms of the formation of the heterostructures.

2. Materials and Methods

Chemicals: cesium carbonate (Cs_2CO_3; Aldrich, CAS No. 534-17-8), octanoic acid (OTAc; Aldrich, CAS No. 124-07-2), lead bromide ($PbBr_2$; Aldrich, CAS No. 10031-22-8), tetraoctylammonium bromide (TOAB; Aldrich, CASNo. 14866-33-2), and didodecyldimethylammonium bromide (DDAB; Aldrich, CAS No. 3282-73-3). Toluene, ethyl acetate, and n-hexane were of analytical grade. Au powders (99.995%, Alfa Aesar, CAS No. 7440-57-5), Ag powders (99.9%, Aldrich, CAS No. 7440-22-4), and nitric acid (HNO_3 70%, BDH, CAS No. 7697-37-2) were used. All chemicals were used without any further purification. Ultrapure water (18.2 MΩ·cm) was produced with a Milli-Q Millipore water purification system.

2.1. Synthesis and Purification of $CsPbBr_3$ NCs

The synthesis and purification of $CsPbBr_3$ NCs were performed based on previous reports [27]. First, the cesium precursor was prepared by loading 1 mmol of Cs_2CO_3 and 10 mL of OTAc into a 20 mL vial, then the mixture was stirred for 10 min at room temperature. The $PbBr_2$ precursor solution was prepared by dissolving 1 mmol of $PbBr_2$ and 2 mmol of TOAB in 10 mL of toluene. For the synthesis of $CsPbBr_3$ NCs, 1.0 mL of a cesium precursor solution was swiftly added to 9 mL of a $PbBr_2$–toluene solution in the conical flask. The reaction was magnetically stirred for 5 min at room temperature in open

air. Subsequently, 3 mL of DDAB (in toluene 10 mg/mL) solution was added. After 2 min, ethyl acetate was added to the crude solution at a volume ratio of 2:1; the precipitate was collected separately after centrifugation and dispersed in toluene. The extra ethyl acetate was added into the toluene dispersion and the precipitate was collected and re-dispersed in n-hexane.

2.2. Synthesis of NP Au

2.2.1. Precursor Alloy Fabrication

Au and Ag powders were mixed at a ratio of 30:70. 2 g of the mixture were ball milled in a SPEX 8000M Mixer/Mill ball mill for 16 h in a hardened steel vial with two hardened steel spheres measuring 8 g each. The powders were homogenized every 30 min in the first 2 h and then every 5 h.

2.2.2. NP Au Fabrication

NP Au powders were prepared via chemical dealloying in HNO_3 70% for 24 h [28,29]. The powders were washed in Milli-Q water 5 times and then dried under vacuum.

2.3. Synthesis and Purification of $CsPbBr_3$–Au Hybrid Structure

$CsPbBr_3$-Au hybrid structures were prepared following two different procedures.

In procedure 1, 70 mg of NP Au was added into the $CsPbBr_3$ NCs (2 mg/mL) dispersed in hexane (3 mL) under ambient conditions. After stirring for 4 h, the powder was filtered and washed several times with hexane under vacuum and then dried overnight.

In procedure 2, the synthesis of $CsPbBr_3$ NCs was repeated in the presence of NP Au. NP Au (140 mg) was added to the $PbBr_2$ precursor solution, then the synthesis proceeded identically. The hexane dispersion was filtered and washed several times with hexane under vacuum, to separate the nanocrystals not linked to gold, and then dried overnight.

2.4. Characterization

X-ray measurements were performed with a Bruker D8 Advance diffractometer operating at 30 kV and 20 mA, equipped with a Cu tube (λ = 1.5418 Å) and a Vantec-1 PSD detector. The powder patterns were recorded in the $10^\circ \leq 2\theta \leq 70^\circ$ range.

Raman measurements were collected using an MS750 spectrograph (sol-instruments) equipped with 600 gr/mm grating. The laser beam (785 nm) was focalized through an Olympus objective (10×), with a laser power of about 7.5 mW. Measurements were performed at room temperature, with a spectral resolution of 1 cm^{-1}.

Time-resolved photoluminescence (TR-PL) measurements were recorded by exciting the samples with 200 fs pulses sourced from an optical parametric amplifier (Light Conversion TOPAS-C) pumped by a regenerative Ti–sapphire amplifier (Coherent Libra-HE). The repetition frequency was 1 kHz and the TR-PL signal was recorded by a streak camera (Hamamatsu C10910) equipped with a grating spectrometer (Princeton Instruments Acton Spectra Pro SP-2300). All measurements were collected in the front-face configuration to reduce inner filter effects. Proper emission filters were applied to remove the reflected contribution of the excitation light.

Scanning electron microscopy (SEM) of nanoporous gold was performed using an FEI Quanta Field Emission Electron Microscope, equipped with an Everhart–Thornley secondary electron detector. Imaging was performed at an operating voltage of 20 kV 10 mm from the examined samples.

SEM studies of heterostructures were carried out using a Carl ZEISS Auriga microscope equipped with an energy-dispersive X-ray spectroscopy (EDX) detector or an ESEM FEI Quanta 200 microscope operating at 25 kV.

TEM measurements on $CsPbBr_3$ NCs and on the heterostructure were performed using a TEM JeolJEM 1400 Plus transmission electron microscope (120 kV).

3. Results and Discussion

An SEM image of the as-prepared NP Au is shown in Figure 1a. The NP Au shows a fine nanoporous structure of interconnected ligaments and pores with a mean diameter of around 20 nm. The $CsPbBr_3$ nanocrystals were synthesized following a room-temperature procedure, as adopted in previous reports, where the effects of the three ligands contibute to their stability over several months [27]. TOAB is used to increase the solubility of $PbBr_2$, while DDAB and OTAc act as capping agents, which promote the uniform dispersion of NCs in hexane and the stability of the compound. The nanocrystals show a uniform morphology with a crystal size of about 15 nm, as shown in Figure 1b.

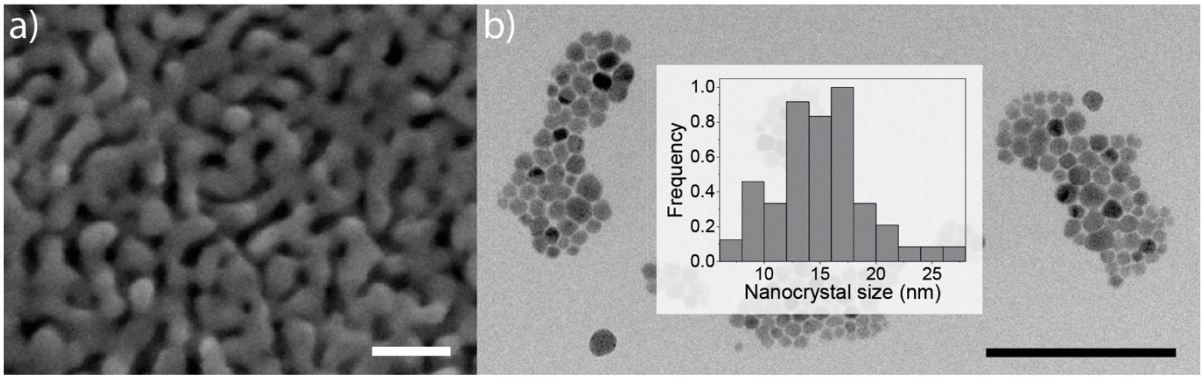

Figure 1. (**a**) SEM image of nanoporous Au; scale bar: 100 nm. (**b**) TEM image of $CsPbBr_3$ NCs; scale bar 200 nm; in the inset is the size distribution of $CsPbBr_3$ nanocrystals.

X-ray diffraction measurements were performed on a nanocrystal precipitate. Figure 2 reports the Rietveld refinement of the pattern obtained using MAUD software [30]. The $CsPbBr_3$ NCs are in the orthorhombic γ-phase (Pbnm, space group No. 62, COD ID 1533062), with lattice parameters a = 8.219 Å, b = 8.254 Å, and c = 11.753 Å.

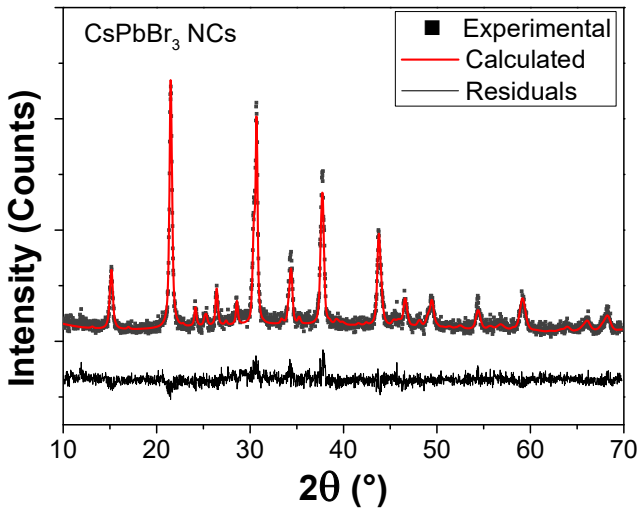

Figure 2. Rietveld refinement of the nanocrystals precipitate. Note: ■ refers to the experimental pattern, the red line is the pattern calculated via Rietveld refinement, while the black line shows the residuals between the experimental and calculated patterns.

In Figure 3, the Raman spectrum of the nanocrystal precipitate is reported; in the inset is an enlarged view of the region covering 200–400 cm^{-1}. The Raman features confirm that $CsPbBr_3$ NCs are in the orthorhombic γ-phase, with an intense peak in the region of 60–80 cm^{-1}, a low-intensity peak around 130 cm^{-1}, and a broad second-order peak around 310 cm^{-1} [31,32].

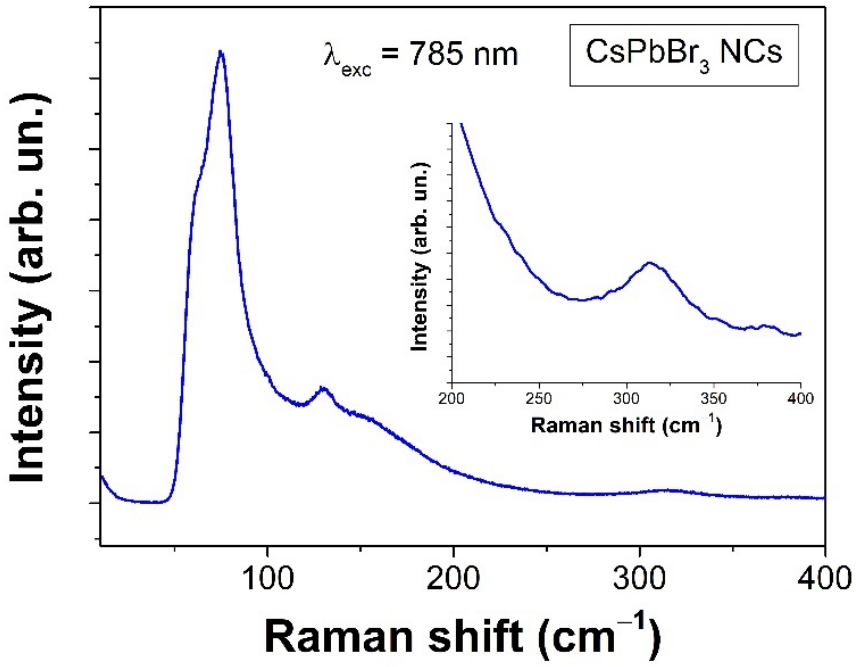

Figure 3. Raman spectrum of nanocrystal precipitate; in the inset is a magnified view of the region of 200–400 cm^{-1}. Note: λ_{exc} = 785 nm.

Figure 4 presents the absorption and emission spectra of colloidal $CsPbBr_3$ dispersed in hexane. The NCs show bright photoluminescence with an emission maximum at 518 nm.

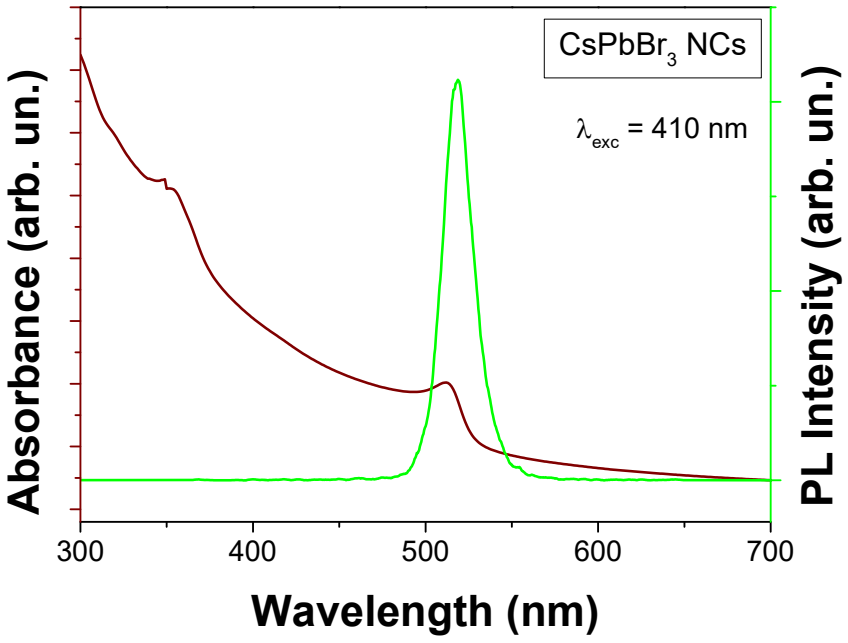

Figure 4. Absorption (brown) and emission (green) spectra of colloidal $CsPbBr_3$ NCs; λ_{exc} = 410 nm.

The synthesis of NCs@NP Au followed two different procedures (detailed conditions are reported in Section 2.3). In procedure 1, a known amount of NP Au (70 mg) was incorporated into the hexane suspension of $CsPbBr_3$ NCs under ambient conditions. The concentration of the $CsPbBr_3$ NCs was 2 mg/mL. Figure 5 shows the pictures of the solution under UV light (375 nm), before and after the addition of NP Au.

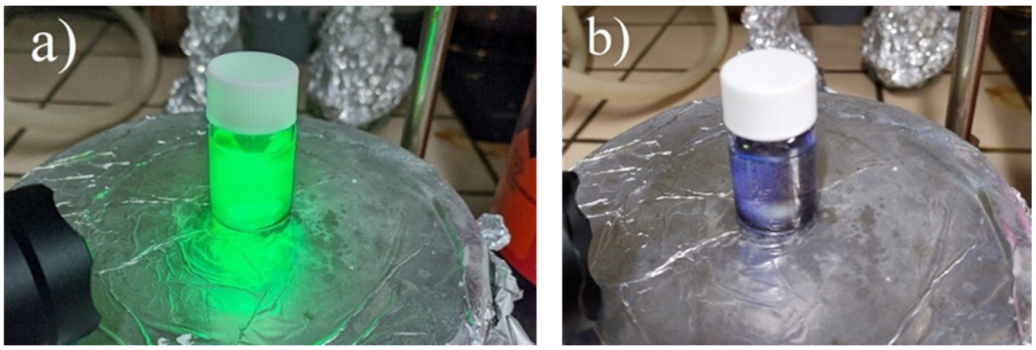

Figure 5. Photographs under UV light (375 nm) of the $CsPbBr_3$ NCs dispersion (**a**) before and (**b**) after the introduction of nanoporous gold.

Above, the solution turns colorless with a drastic quenching of the fluorescence; the slight blue fluorescence is due to the glass vial. The Raman measurements (Figure 6) show the disappearance of the features typical of γ-$CsPbBr_3$ and the appearance of two peaks (135 and 176 cm^{-1}), which cannot be assigned but are in the range of Cs-Pb-Br vibrations [31,33,34]. This can be attributed to the instability of NCs in the presence of gold. Balakrishnan et al. already reported the instability of $CsPbBr_3$ NCs in the presence of gold, depending on the procedure followed for the synthesis of the heterostructure, evidencing the degradation of perovskites in 5 min after the addition of gold NPs in a solution of colloidal $CsPbBr_3$ NCs [35].

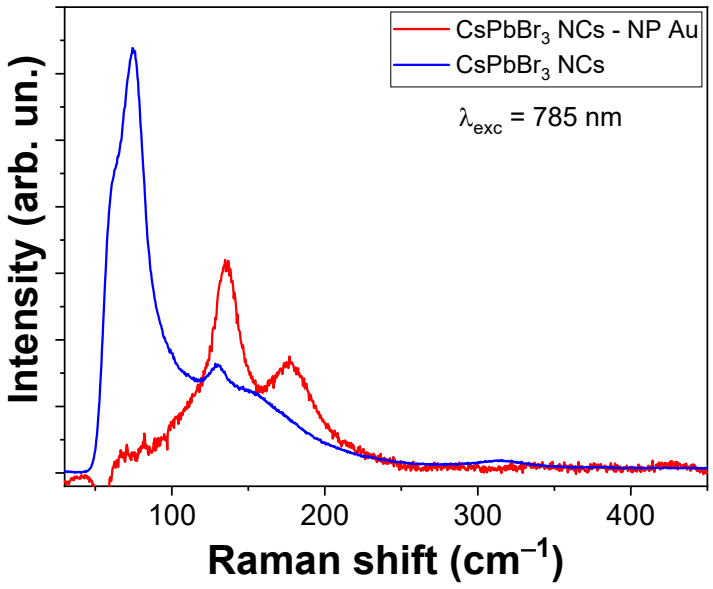

Figure 6. Raman spectrum of NP Au soaked with $CsPbBr_3$ NCs (red) compared with pure $CsPbBr_3$ NCs (blue).

The capping agent (namely DDAB) is formed by the alkyl chain terminating with the nitrogen and methyl groups. It is widely accepted that there is a strong affinity of the Au surface with ammonium surfactants, and the capping agent likely leaves the nanoparticles to deposit on the Au nanostructures [36–38].

We argue that NP Au possesses a good affinity with the capping agent of $CsPbBr_3$ NCs. Stripped of all protection, NCs are no longer stable in hexane and degrade in different stoichiometric phases, as observed in the Raman spectra. To further confirm the hypothesis, the Au nanostructures were covered with the same capping agent and successively added to the $CsPbBr_3$ NCs hexane solution. No interaction between $CsPbBr_3$ NCs and Au nanostructures was observed in this case; the perovskites maintained the structural

stability and their characteristic optical properties. To further confirm the hypothesis of the degradation, we performed an elemental analysis on different points of the surface of the sample obtained with procedure 1, using SEM-EDX measurements (Table 1). Paying attention to Cs, Pb and Br percentages, we evidenced the presence of lead or cesium or both, with the disappearance of bromine. This difference in the stoichiometry from the starting $CsPbBr_3$ NCs confirms the absence of perovskites and the formation of amorphous Cs-Pb compounds.

Table 1. SEM–EDX measurements on NP Au soaked with $CsPbBr_3$ NCs.

Element	Line Type	Atom %	Atom % Error
C K	K	41.9	0.9
N K	K	23.2	2.6
O K	K	14.0	1.4
Ag L	L	1.0	0.1
Cs L	L	0.5	0.1
Au L	L	18.9	0.2
Pb L	L	0.5	0.1
		100.0	

In procedure 2, nanoporous gold was added during the synthesis of $CsPbBr_3$ nanocrystals, then the synthesis proceeded as mentioned in Section 2.1. Figure 7 reports the XRD pattern of the NC–NP Au sample compared to pure NP Au. It is possible to notice the presence of additional peaks (at 21.5°, 31.5°, 49.4° and 59.1°) pertaining to pure $CsPbBr_3$ NCs (Rietveld refinement in Figure 2).

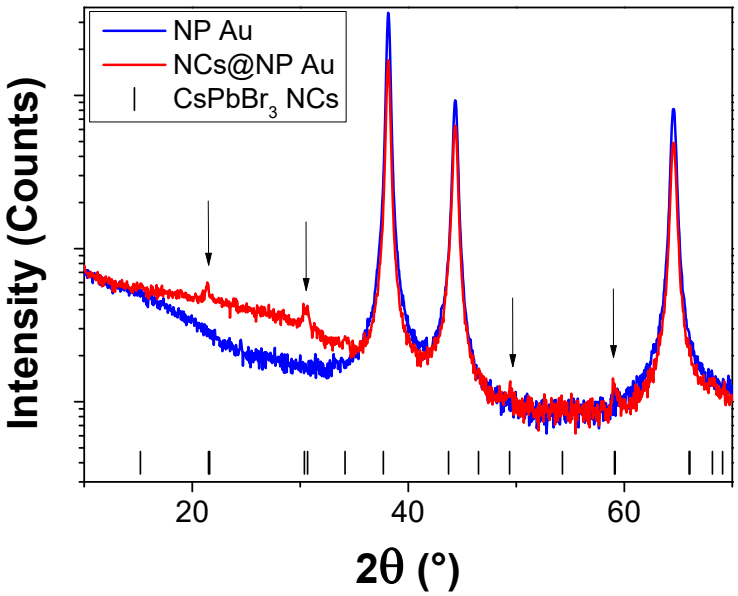

Figure 7. XRD pattern of the sample of pure NP Au (blue) and the NCs@NP Au heterostructure (red). The vertical bar individuates the main peaks of pure $CsPbBr_3$ NCs.

In order to confirm the success of the procedure and exclude the presence of degradation products, we performed SEM-EDX measurements on 6 different areas. The composition was found to be homogeneous across the sample surface, and Table 2 reports the atomic percentages of the elements detected in one of these areas, evidencing the correct stoichiometry of $CsPbBr_3$ NCs.

Table 2. SEM–EDX measurements on $CsPbBr_3$ NCs@NP Au sample.

Element	Line Type	Atom %	Atom % Error
C K	K	37.4	0.8
N K	K	19.9	2.1
O K	K	15.8	1.3
Br K	K	3.3	0.2
Ag L	L	4.9	0.1
Cs L	L	1.1	0.1
Au L	L	16.7	0.2
Pb L	L	0.9	0.1
		100.0	

Figure 8 reports the TEM images of the NP Au and the hybrid structure with perovskites. The resolution of the images is affected by the nature of the material itself; NP Au powders have μm-range mean sizes, and for this reason it was only possible to acquire images of the smallest Au particles (around 200 nm in size), which were partially transparent to the electron beam. The thickness of the particles was still high for TEM imaging, which caused the low resolution of the images. However, looking at a small grain of NP Au in Figure 8b, the presence of the NCs at the surface of the gold structure is clearly visible, evidencing the close contact between the Au and $CsPbBr_3$ NCs.

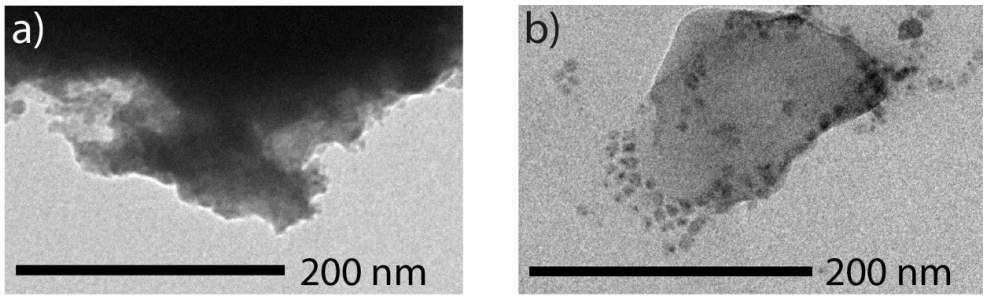

Figure 8. TEM images of NP Au (**a**) and the NC–NP Au hybrid structure (**b**).

Figure 9 shows the steady-state luminescence spectrum of the NCs@NP Au heterostructure compared to the emission of the pure $CsPbBr_3$ NCs.

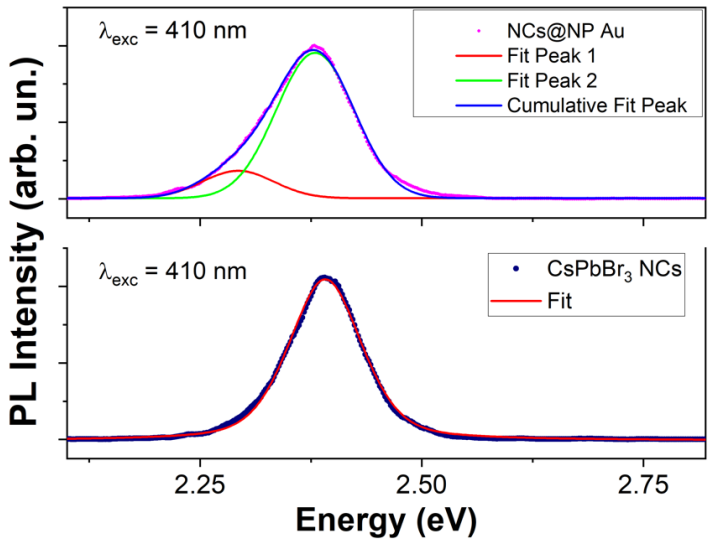

Figure 9. Steady-state luminescence spectra of pure $CsPbBr_3$ NCs and the NCs–NP Au hybrid structure; λ_{exc} = 410 nm.

The curves were fitted with a pseudo-Voigt function, a combination of Gaussian and Lorentzian profiles:

$$I = I_0 + A\left[\mu\frac{2}{\pi}\frac{w_L}{4(x-x_c)^2+w_L^2} + (1-\mu)\frac{\sqrt{4\ln(2)}}{\sqrt{\pi}w_G}e^{-\frac{4\ln(2)}{w_G^2}(x-x_c)^2}\right] \quad (1)$$

where μ represents the Lorentzian character of the Voigt profile, and w_L and w_G are the width parameters of the Lorentzian and Gaussian components, respectively. Comparing the PL behavior of the NCs@NP Au sample and pure $CsPbBr_3$ NCs, it is possible to observe a slight red shift of the main peak at 518 nm (2.39 eV) and the appearance of a new less-intense peak at lower energies. The derived parameters are reported in Table 3.

Table 3. Fit parameters of PL measurements on pure $CsPbBr_3$ NCs and the NCs-Au hybrid structure.

Sample	Peak	x_c [eV]	w [eV]
$CsPbBr_3$ NCs		2.39	0.097
NCs@NP Au	Peak 1	2.37	0.088
	Peak 2	2.29	0.081

The variation in the positions of the peak implies an influence of the nanoporous gold matrix on the excited-state properties of $CsPbBr_3$ NCs. The possible reason for the appearance of the secondary peak could be the formation of NCs with different dimensions. Effectively, the synthesis procedure promotes the formation of NCs with dimensions of around 15 nm, although we cannot exclude the formation of aggregation or bigger nanocrystals inside the gold pores.

The time-resolved photoluminescence measurements (reported in Figure 10) performed on the samples give more insight into the properties of the recombination mechanism. With regard to the NCs@NP Au sample, the two peaks show the same decay behavior. For this reason, only one curve is reported for this sample in Figure 10. The curves are fitted with a biexponential decay function:

$$I(t) = I_0 + \sum_{i=1}^{2} A_i e^{-(t-t_0)/\tau_i} \quad (2)$$

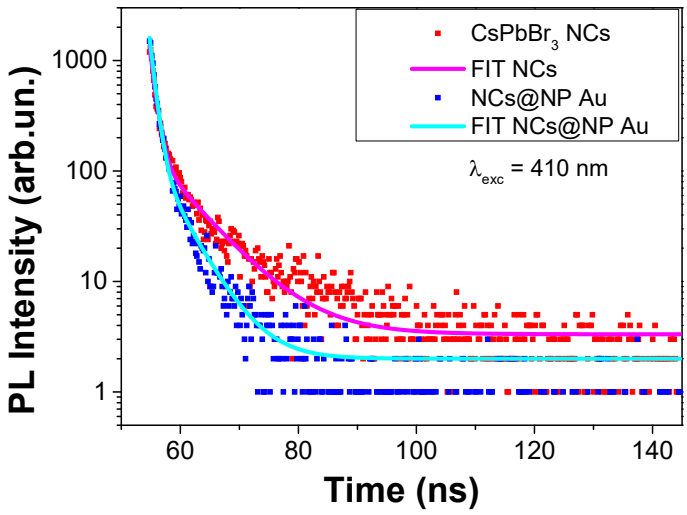

Figure 10. Time-resolved photoluminescence measurements of pure $CsPbBr_3$ NCs and the NCs–NP Au hybrid structure; λ_{exc} = 410 nm.

Here, $I(t)$ is the time-dependent PL intensity, I_0 is the initial PL intensity, A_i is the amplitude, t is time, t_0 is the initial time, and τ_i is the characteristic lifetime. The average lifetime is calculated using the following relation [39]:

$$\overline{\tau} = \frac{\sum_i A_i \cdot \tau_i^2}{\sum_i A_i \cdot \tau_i} \quad (3)$$

The error in parameter A_i derives from the fit, whilst in the case of τ_i it is an experimental error resulting from the rising time, which is higher than the error provided by the fit. The error of the average lifetime is calculated by the propagation of uncertainties. Table 4 shows the fitting parameters, showing that $CsPbBr_3$ NCs are characterized by the presence of two decay components. Previous studies assigned the fast time component to the trap-assisted recombination and the long one to the intrinsic electron–hole recombination [40,41].

Table 4. Fit parameters of TR photoluminescence measurements.

Sample	$\overline{\tau}$ [ns]	A_1	τ_1 [ns]	A_2	τ_2 [ns]
$CsPbBr_3$ NCs	3.6 (8)	1445 (1)	0.9 (6)	144 (1)	7.0 (6)
NCs@NP Au	1.9 (3)	1760 (1)	0.9 (6)	140 (1)	4.4 (6)

When $CsPbBr_3$ NCs are grown in the presence of NP Au, the average lifetime decreases from 3.6 ns to 1.9 ns, suggesting an interaction between $CsPbBr_3$ NCs and the nanoporous gold matrix, as evidenced by the shortening of the average lifetime with respect to the $CsPbBr_3$ NCs. Indeed, a faster decay time can be considered an indication of the formation of the NC–NP Au hybrid structure with the presence of a non-radiative recombination path and an interfacial charge transfer [14,35,42,43]. Actually, the same results could be due to other effects, such as the formation of surface defects, although the formation of a defective structure does not explain the high stability and the absence of a new feature, while an energy transfer is more likely, as already observed in other $CsPbBr_3$ NCs-Au systems [35]. The transfer efficiency can be calculated by the following relation:

$$\eta = 1 - \frac{\tau}{\tau_0} \quad (4)$$

where τ_0 is the average lifetime in pure $CsPbBr_3$ NCs and τ is the average lifetime in the presence of gold. The calculated charge transfer efficiency is around 47%.

4. Conclusions

In summary, the goal of this study was to achieve a $CsPbBr_3$-Au heterostructure. In one approach, $CsPbBr_3$ NCs dispersed in hexane were mixed with nanoporous gold. The result was the disappearance of the luminescence, the cause of which was assumed to be the degradation of NCs and the subsequent formation of amorphous compounds. The second approach involved the synthesis of NCs directly on the NP Au surface. In this case, it was possible to notice a red shift in the emission spectrum and a faster decay rate. Such behavior can be attributed to the achievement of a nanostructure of $CsPbBr_3$ NCs and NP Au, with an efficient charge transfer rate. The results showed the high potential for applications where an efficient charge transfer is required. Further, the use of perovskite NCs as an efficient sensitizer strongly suggests the possibility to achieve tunable photocatalytic devices active across the visible range. In this regard, further specific experimental tests need to be performed.

Author Contributions: Conceptualization, J.S., P.C.R. and A.P.; methodology, J.S., P.C.R. and A.P.; validation, C.M.C., D.C. and L.S.; formal analysis, J.S., A.P. and P.C.R.; investigation, C.M.C., D.C.,

Q.A.A. and L.S.; writing—original draft preparation, J.S., A.P. and P.C.R.; writing—review and editing, J.S., A.P., P.C.R., Q.A.A., G.P. and L.P.; visualization, J.S. and P.C.R.; supervision, P.C.R. and L.P.; project administration, P.C.R.; funding acquisition, G.P. and P.C.R. All authors have read and agreed to the published version of the manuscript.

Funding: Financial support from Fondazione di Sardegna, for both projects ADVANCING, CUP F72F20000360007, and L.R 7. CUP F74I19000930007, "NG-Light: A New Generation of Phosphors", is gratefully acknowledged.

Institutional Review Board Statement: Not applicable.

Informed Consent Statement: Not applicable.

Data Availability Statement: The datasets generated or analyzed during the current study are available from the corresponding author on reasonable request.

Acknowledgments: The authors are grateful to Ten. Col. Cesare Vecchio Comandante del Reparto Investigazioni Scientifiche di Cagliari, Magg. Marco Palanca Comandante della Sezione di Chimica, Esplosivi ed Infiammabili and Mar. Ord. Claudia Melis Analista di laboratorio in Microscopia Elettronica for SEM imaging. The authors acknowledge the CeSAR (Centro Servizi d'Ateneo per la Ricerca) of the University of Cagliari, Italy, for the time-resolved photoluminescence experiments and TEM measurements. One of the authors (A.P.) performed his activity within the framework of the International Ph.D. in Innovation Sciences and Technologies at the University of Cagliari, Italy.

Conflicts of Interest: The authors declare no conflict of interest.

References

1. Protesescu, L.; Yakunin, S.; Bodnarchuk, M.I.; Krieg, F.; Caputo, R.; Hendon, C.H.; Yang, R.X.; Walsh, A.; Kovalenko, M.V. Nanocrystals of Cesium Lead Halide Perovskites (CsPbX 3, X = Cl, Br, and I): Novel Optoelectronic Materials Showing Bright Emission with Wide Color Gamut. *Nano Lett.* **2015**, *15*, 3692–3696. [CrossRef] [PubMed]
2. Shaikh, J.S.; Shaikh, N.S.; Mali, S.S.; Patil, J.V.; Beknalkar, S.A.; Patil, A.P.; Tarwal, N.L.; Kanjanaboos, P.; Hong, C.K.; Patil, P.S. Quantum Dot Based Solar Cells: Role of Nanoarchitectures, Perovskite Quantum Dots, and Charge-Transporting Layers. *ChemSusChem* **2019**, *12*, 4724–4753. [CrossRef] [PubMed]
3. Zhang, J.; Zhang, W.; Cheng, H.-M.; Silva, S.R.P. Critical review of recent progress of flexible perovskite solar cells. *Mater. Today* **2020**, *39*, 66–88. [CrossRef]
4. Zhou, Y.; Zhao, Y. Chemical stability and instability of inorganic halide perovskites. *Energy Environ. Sci.* **2019**, *12*, 1495–1511. [CrossRef]
5. Satta, J.; Casu, A.; Chiriu, D.; Carbonaro, C.M.; Stagi, L.; Ricci, P.C. Formation Mechanisms and Phase Stability of Solid-State Grown CsPbI3 Perovskites. *Nanomaterials* **2021**, *11*, 1823. [CrossRef]
6. Cho, H.; Kim, Y.-H.; Wolf, C.; Lee, H.-D.; Lee, T.-W. Improving the Stability of Metal Halide Perovskite Materials and Light-Emitting Diodes. *Adv. Mater.* **2018**, *30*, 1704587. [CrossRef]
7. Satta, J.; Melis, C.; Carbonaro, C.M.; Pinna, A.; Salado, M.; Salazar, D.; Ricci, P.C. Raman spectra and vibrational analysis of CsPbI3: A fast and reliable technique to identify lead halide perovskite polymorphs. *J. Mater.* **2021**, *7*, 127–135. [CrossRef]
8. Dimitrijević, N.M.; Rajh, T.; Ahrenkiel, S.P.; Nedeljković, J.M.; Mićić, O.I.; Nozik, A.J. Charge Separation in Heterostructures of InP Nanocrystals with Metal Particles. *J. Phys. Chem. B* **2005**, *109*, 18243–18249. [CrossRef]
9. Sheldon, M.T.; Trudeau, P.-E.; Mokari, T.; Wang, L.-W.; Alivisatos, A.P. Enhanced Semiconductor Nanocrystal Conductance via Solution Grown Contacts. *Nano Lett.* **2009**, *9*, 3676–3682. [CrossRef]
10. Nawrot, K.C.; Wawrzyńczyk, D.; Bezkrovnyi, O.; Kępiński, L.; Cichy, B.; Samoć, M.; Nyk, M. Functional CdS-Au Nanocomposite for Efficient Photocatalytic, Photosensitizing, and Two-Photon Applications. *Nanomaterials* **2020**, *10*, 715. [CrossRef]
11. Wei, H.; Ratchford, D.; Li, X.; Xu, H.; Shih, C.-K. Propagating Surface Plasmon Induced Photon Emission from Quantum Dots. *Nano Lett.* **2009**, *9*, 4168–4171. [CrossRef] [PubMed]
12. Dey, S.; Zhao, J. Plasmonic Effect on Exciton and Multiexciton Emission of Single Quantum Dots. *J. Phys. Chem. Lett.* **2016**, *7*, 2921–2929. [CrossRef] [PubMed]
13. Carretero-Palacios, S.; Jiménez-Solano, A.; Míguez, H. Plasmonic Nanoparticles as Light-Harvesting Enhancers in Perovskite Solar Cells: A User's Guide. *ACS Energy Lett.* **2016**, *1*, 323–331. [CrossRef]
14. Liao, J.-F.; Cai, Y.-T.; Li, J.-Y.; Jiang, Y.; Wang, X.-D.; Chen, H.-Y.; Kuang, D.-B. Plasmonic CsPbBr3–Au nanocomposite for excitation wavelength dependent photocatalytic CO_2 reduction. *J. Energy Chem.* **2021**, *53*, 309–315. [CrossRef]
15. Zhou, X.; Bao, C.; Li, F.; Gao, H.; Yu, T.; Yang, J.; Zhu, W.; Zou, Z. Hole-transport-material-free perovskite solar cells based on nanoporous gold back electrode. *RSC Adv.* **2015**, *5*, 58543–58548. [CrossRef]
16. Ding, Y.; Zhang, Z. Introduction to nanoporous metals. In *Nanoporous Metals for Advanced Energy Technologies*; Springer International Publishing: Cham, Switzerland, 2016; pp. 1–35.

17. Law, M.; Greene, L.E.; Johnson, J.C.; Saykally, R.; Yang, P. Nanowire dye-sensitized solar cells. *Nat. Mater.* **2005**, *4*, 455–459. [CrossRef]
18. Ye, M.; Xin, X.; Lin, C.; Lin, Z. High efficiency dye-sensitized solar cells based on hierarchically structured nanotubes. *Nano Lett.* **2011**, *11*, 3214–3220. [CrossRef]
19. Zhang, W.; Zhao, Y.; He, K.; Luo, J.; Li, G.; Liu, R.; Liu, S.; Cao, Z. Ultrathin nanoporous metal—semiconductor heterojunction photoanodes for visible light hydrogen evolution. *Nano Res.* **2018**, *11*, 2046–2057. [CrossRef]
20. Zielasek, V.; Jürgens, B.; Schulz, C.; Biener, J.; Biener, M.M.; Hamza, A.V.; Bäumer, M. Gold Catalysts: Nanoporous Gold Foams. *Angew. Chemie Int. Ed.* **2006**, *45*, 8241–8244. [CrossRef]
21. Ruffino, F.; Grimaldi, M.G. Nanoporous Gold-Based Sensing. *Coatings* **2020**, *10*, 899. [CrossRef]
22. Kucheyev, S.O.; Hayes, J.R.; Biener, J.; Huser, T.; Talley, C.E.; Hamza, A.V. Surface-enhanced Raman scattering on nanoporous Au. *Appl. Phys. Lett.* **2006**, *89*, 053102. [CrossRef]
23. Zhang, L.; Song, Y.; Fujita, T.; Zhang, Y.; Chen, M.; Wang, T.-H. Large Enhancement of Quantum Dot Fluorescence by Highly Scalable Nanoporous Gold. *Adv. Mater.* **2014**, *26*, 1289–1294. [CrossRef] [PubMed]
24. Biener, J.; Wittstock, A.; Zepeda-Ruiz, L.A.; Biener, M.M.; Zielasek, V.; Kramer, D.; Viswanath, R.N.; Weissmüller, J.; Bäumer, M.; Hamza, A.V. Surface-chemistry-driven actuation in nanoporous gold. *Nat. Mater.* **2008**, *8*, 47–51. [CrossRef] [PubMed]
25. Gonçalves, J.M.; Kumar, A.; da Silva, M.I.; Toma, H.E.; Martins, P.R.; Araki, K.; Bertotti, M.; Angnes, L. Nanoporous Gold-Based Materials for Electrochemical Energy Storage and Conversion. *Energy Technol.* **2021**, *9*, 2000927. [CrossRef]
26. Jia, C.; Yin, H.; Ma, H.; Wang, R.; Ge, X.; Zhou, A.; Xu, X.; Ding, Y. Enhanced photoelectrocatalytic activity of methanol oxidation on TiO_2-decorated nanoporous gold. *J. Phys. Chem. C* **2009**, *113*, 16138–16143. [CrossRef]
27. Song, J.; Li, J.; Xu, L.; Li, J.; Zhang, F.; Han, B.; Shan, Q.; Zeng, H. Room-Temperature Triple-Ligand Surface Engineering Synergistically Boosts Ink Stability, Recombination Dynamics, and Charge Injection toward EQE-11.6% Perovskite QLEDs. *Adv. Mater.* **2018**, *30*, 1800764. [CrossRef]
28. McCue, I.; Benn, E.; Gaskey, B.; Erlebacher, J. Dealloying and Dealloyed Materials. *Annu. Rev. Mater. Res.* **2016**, *46*, 263–286. [CrossRef]
29. Pia, G.; Mascia, M.; Delogu, F. Kinetics of nanoporous Au formation by chemical dealloying. *Scr. Mater.* **2014**, *76*, 57–60. [CrossRef]
30. Lutterotti, L. Total pattern fitting for the combined size–strain–stress–texture determination in thin film diffraction. *Nucl. Instrum. Methods Phys. Res. Sect. B Beam Interact. Mater. At.* **2010**, *268*, 334–340. [CrossRef]
31. Qin, Z.; Dai, S.; Hadjiev, V.G.; Wang, C.; Xie, L.; Ni, Y.; Wu, C.; Yang, G.; Chen, S.; Deng, L.; et al. Revealing the Origin of Luminescence Center in 0D Cs 4 PbBr 6 Perovskite. *Chem. Mater.* **2019**, *31*, 9098–9104. [CrossRef]
32. Yaffe, O.; Guo, Y.; Tan, L.Z.; Egger, D.A.; Hull, T.; Stoumpos, C.C.; Zheng, F.; Heinz, T.F.; Kronik, L.; Kanatzidis, M.G.; et al. Local Polar Fluctuations in Lead Halide Perovskite Crystals. *Phys. Rev. Lett.* **2017**, *118*, 136001. [CrossRef] [PubMed]
33. Liu, M.; Zhao, J.; Luo, Z.; Sun, Z.; Pan, N.; Ding, H.; Wang, X. Unveiling Solvent-Related Effect on Phase Transformations in CsBr–PbBr 2 System: Coordination and Ratio of Precursors. *Chem. Mater.* **2018**, *30*, 5846–5852. [CrossRef]
34. Xie, L.-Q.; Zhang, T.-Y.; Chen, L.; Guo, N.; Wang, Y.; Liu, G.-K.; Wang, J.-R.; Zhou, J.-Z.; Yan, J.-W.; Zhao, Y.-X.; et al. Organic–inorganic interactions of single crystalline organolead halide perovskites studied by Raman spectroscopy. *Phys. Chem. Chem. Phys.* **2016**, *18*, 18112–18118. [CrossRef] [PubMed]
35. Balakrishnan, S.K.; Kamat, P.V. Au–CsPbBr 3 Hybrid Architecture: Anchoring Gold Nanoparticles on Cubic Perovskite Nanocrystals. *ACS Energy Lett.* **2017**, *2*, 88–93. [CrossRef]
36. Xiao, J.; Qi, L. Surfactant-assisted, shape-controlled synthesis of gold nanocrystals. *Nanoscale* **2011**, *3*, 1383. [CrossRef]
37. Millstone, J.E.; Hurst, S.J.; Métraux, G.S.; Cutler, J.I.; Mirkin, C.A. Colloidal Gold and Silver Triangular Nanoprisms. *Small* **2009**, *5*, 646–664. [CrossRef]
38. Muniba; Naz, G.; Anjum, M.N.; Irfan, M.; Irfan, M.; Arshad, M.; Bajwa, S.Z.; Khan, W.S. Quats stabilized gold nanospheres for efficient ligand exchange procedure. *Results Mater.* **2020**, *5*, 100065. [CrossRef]
39. Lakowicz, J.R. *Principles of Fluorescence Spectroscopy*; Lakowicz, J.R., Ed.; Springer: Boston, MA, USA, 2006; ISBN 978-0-387-31278-1.
40. Luo, B.; Pu, Y.C.; Yang, Y.; Lindley, S.A.; Abdelmageed, G.; Ashry, H.; Li, Y.; Li, X.; Zhang, J.Z. Synthesis, Optical Properties, and Exciton Dynamics of Organolead Bromide Perovskite Nanocrystals. *J. Phys. Chem. C* **2015**, *119*, 26672–26682. [CrossRef]
41. Wu, K.; Liang, G.; Shang, Q.; Ren, Y.; Kong, D.; Lian, T. Ultrafast interfacial electron and hole transfer from CsPbBr3 perovskite quantum dots. *J. Am. Chem. Soc.* **2015**, *137*. [CrossRef]
42. Wu, Y.; Han, Q.; Wang, M.; Juan, F.; Hou, G.; Xun, F.; Wei, H.; Xu, J.; Cao, B. Enhanced photoluminescence of CsPbBr 3-x I x nanocrystals via plasmonic Au nanoarrays. *Opt. Express* **2021**, *29*, 36988–36996. [CrossRef]
43. Chen, S.; Lyu, D.; Ling, T.; Guo, W. Reversible modulation of CsPbBr3 perovskite nanocrystal/gold nanoparticle heterostructures. *Chem. Commun.* **2018**, *54*, 4605–4608. [CrossRef] [PubMed]